Supporting Information for

Molecular Press-Annealed Phase-Pure 2D/3D Heterojunctions with Hydrophobic Interfaces for Stable Perovskite Solar Cells

Runquan Qi,[a†] Guiran Gao,[a†] Gang Wang,[b†] Aijie Zhou,[a] Guichuan Xing,[b] Ke Guo,*[a] Runfeng Chen, *[a] Guangbao Wu*[a]

a. State Key Laboratory of Flexible Electronics (LoFE) & Institute of Advanced Materials (IAM), Nanjing University of Posts & Telecommunications, 9 Wenyuan Road, Nanjing 210023, P. R. China.

E-mails: iamkguo@njupt.edu.cn, iamrfchen@njupt.edu.cn., iamgbwu@njupt.edu.cn.

b. Joint Key Laboratory of the Ministry of Education, Institute of Applied Physics and Materials Engineering, University of Macau, Avenida da Universidade, Taipa, Macau 999078, P. R. China.

Experimental Sections

Materials.

Methylamine hydrochloride (MACl) and bathocuproine (BCP) were purchased from Xi'an YuRi Solar Technology Co., Ltd. Formamidinium iodide (FAI), lead iodide (PbI_2), and cesium iodide (CsI) were purchased from Youxuan Technology Co., Ltd. Buckminsterfullerene (C_{60}) and stannic oxide (SnO_2) were purchased from Advanced Election Technology. 4-PADCB were purchased from Suzhou Liwei New Material Co., Ltd. Decylamine (DA) was purchased from Energy Chemical. Isopropanol (IPA), *N,N*-dimethylformamide (DMF), dimethyl sulfoxide (DMSO) and chlorobenzene (CB), and hydroiodic acid (HI, 57 wt%) were all obtained from Sigma-Aldrich. Bathocuproine (BCP) was purchased from Xi'an Baolaite Optoelectronic Technology Co., Ltd.

Synthesis of 2D perovskite single crystals.

2D perovskite single crystals were prepared using a previously reported method with slight modifications. [1] PbO (2232 mg, 10 mmol) was dissolved in 57 wt% aqueous HI (16 mL) by heating to boiling under stirring for 5 min, forming a clear yellow solution. Methylammonium chloride (507 mg, 7.5 mmol) was then added, briefly generating a black precipitate that rapidly dissolved. DA (150 μL, 1.3 mmol), pre-dissolved in 50% aqueous H_3PO_2 (2 mL), was added dropwise. The mixture was left to cool naturally on a hotplate (initially 110 °C) to room temperature. After ~3 h, black plate-like crystals formed, which were collected by vacuum filtration and dried under reduced pressure.

Synthesis of DAI.

Decylammonium iodide (DAI) was synthesized by protonation of 0.415 g of DA with 0.49 mL of 57 wt% aqueous HI in 5 mL of ethanol under ice-bath cooling. The crude product was isolated after solvent removal, purified by recrystallization, washed with diethyl ether, and dried under vacuum prior to use.

Preparation of Perovskite Precursor Solution.

A 1.5 M perovskite precursor solution was prepared by dissolving 19.5 mg of CsI, 219.3 mg of FAI, 23.8 mg of MAI, and 760.7 mg of PbI_2 (with a 10% excess) in 1 mL of a mixed solvent of DMF:DMSO (volume ratio 4:1). The resulting stoichiometry corresponds to $Cs_{0.05}FA_{0.85}MA_{0.1}PbI_3$, giving a perovskite with a bandgap of 1.53 eV. To improve crystallinity and reduce bulk defects, 12.5 mol% MACl and 0.08 mol% PEACl were added to the precursor solution. The mixture was stirred for 2 h until fully dissolved. All solution preparation steps were carried out in a nitrogen-filled glovebox.

Preparation of phase-pure 2D/3D Films.

A DAI solution (4 mg mL^{-1} in isopropanol) was deposited onto a blank ITO substrate by spin-coating at 3,000 rpm for 30 s and then annealed at 100 °C for 10 min. The obtained DAI-coated ITO substrate was brought into conformal contact with a pre-annealed perovskite-coated ITO substrate, followed by molecular press annealing at 150 °C under 2 MPa for 5 min. This treatment triggered an interfacial solid-phase reaction and led to the formation of a 2D/3D perovskite heterojunction.

Device Fabrication.

Patterned ITO substrates were sequentially cleaned with deionized water, acetone, ethanol, and isopropanol, dried under a nitrogen stream, and treated with UV-ozone for 30 min before being transferred into a nitrogen-filled glovebox. A 4-PADCB solution was prepared by dissolving 1 mg of 4-PADCB in ethanol, and 60 μL of the solution was spin-coated onto the ITO substrate at 3000 rpm for 30 s, followed by annealing at 100 °C for 10 min to form the hole-transport layer. The perovskite precursor solution was filtered through a membrane filter and deposited by a two-step spin-coating process at 1,000 rpm for 10 s and 4,000 rpm for 40 s using a volume of 60 μL. During the second step, 200 μL of CB was dripped onto the spinning substrate at 35 s as the antisolvent. The as-deposited yellowish film was then annealed at 100 °C for 30 min. For the heterojunction films, the buried 2D/3D structure was constructed by molecular press annealing as described above. Subsequently, a 10 nm C_{60} layer and a 1 nm BCP layer were sequentially deposited by thermal evaporation under high vacuum at rates of 1 Å s^{-1} and 0.05 Å s^{-1}, respectively. Finally, a 100 nm Ag electrode was thermally evaporated through a shadow mask, affording devices with an active area of 0.045 cm^2 and the architecture of ITO/4-PADCB/perovskite/C_{60}/BCP/Ag.

Electron-only Device Fabrication.

The patterned ITO glasses were cleaned with ultraviolet-ozone (UV-O_3) treatment for 30 minutes. The diluted SnO_2 was deposited onto ITO glasses at 3,000 rpm for 60 s and then heated at 150 °C for 30 min. Perovskite precursor solutions were spin coated on top of SnO_2 at 4,000 rpm for 30 s, followed by annealing at 100 °C for 15 min. Then, $PC_{61}BM$ was spin coated on perovskite at 3,000 rpm for 40 s. Finally, 100 nm Ag was evaporated through a shadow mask with an aperture area of 0.045 cm^2 to serve as the electrode.

Characterizations.

J-V characteristics were measured with a digital source meter (Keithley-2400) under simulated solar illumination at 100 mW cm^{-2} (AM 1.5G) without any device encapsulation. SAN-EI electric solar simulator (XES-50S1) was used for characterization. The SCLC test was carried out in the dark, and the range of scanning voltage was from -0.1 to 3 V. Surface morphology of the perovskite films was characterized by Hitachi S-4800 SEM and Bruker Dimension ICON AFM in tapping mode. Absorption spectra were recorded on a lambda 35 PerkinElmer UV-vis spectrophotometer. Steady-state PL spectra were obtained from Hitachi F-4700 spectrometer (Japan). The TRPL spectra were measured using FLS980 spectrometer (Edinburgh Instruments Ltd.) with the excitation of a 450 nm laser. XRD patterns of perovskite films were measured with a Bruker Model D8 Discover machine. The measurement chamber was equipped with a monochromatic Cu kγ X-ray source. The electrochemical impedance spectroscopy was performed by CHI660E electrochemical workstation (Chenhua Instrument Shanghai Co., Ltd., China). Contact angle characterizations were carried out using droplet shape analyzer (KRÜSS GmbH Germany). The *in-situ* PL spectra of perovskite thin films prepared on ITO were obtained by a photoluminescence spectrometer (Shaanxi Spectral Microvision Co., Ltd.). The PL signals of perovskite films were continuously collected under thermal-annealing condition (at 100 ℃) in the air.

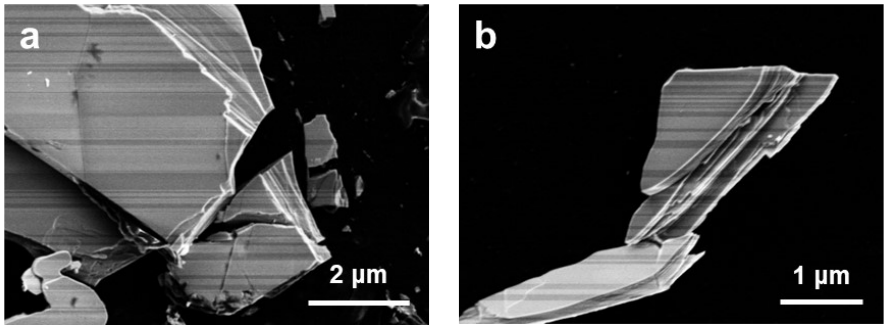

Fig. S1 SEM image of the as-prepared DA/FA-based 2D single crystal.

The well-defined lamellar morphology is characteristic of a 2D layered perovskite structure, where the perovskite layers are separated by organic spacer cations and the interlayer interaction is dominated by van der Waals forces.

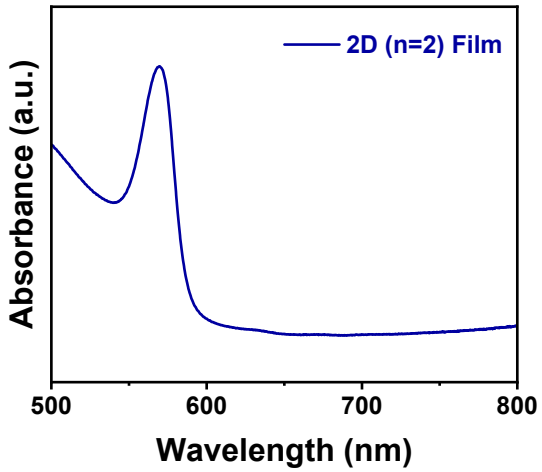

Fig. S2 UV–vis absorption spectrum of the film prepared by spin-coating the precursor solution with the stoichiometric composition of an n = 2 perovskite.

The absorption spectrum shows a single distinct excitonic peak, indicating the formation of a phase-pure n = 2 perovskite without detectable mixed-n phases.

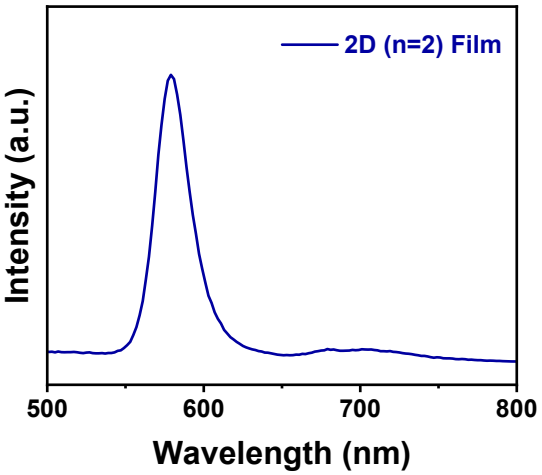

Fig. S3 PL spectrum of the film prepared by spin-coating the precursor solution with the stoichiometric composition of an n = 2 perovskite. The PL spectra were obtained using 450 nm

laser excitation.

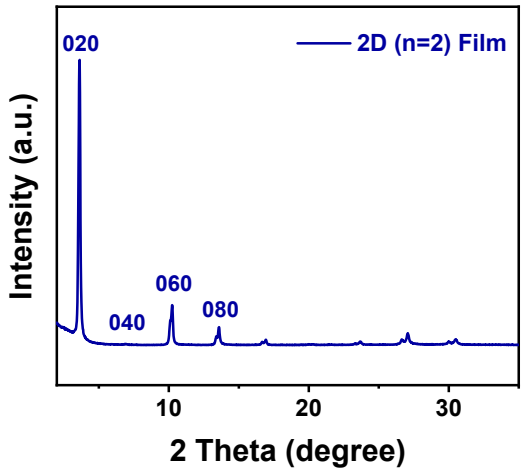

Fig. S4 XRD pattern of the film prepared by spin-coating the precursor solution with the stoichiometric composition of an n = 2 perovskite.

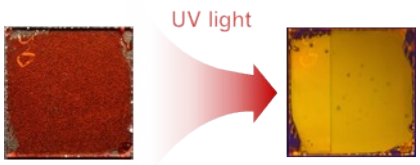

Fig. S5 Digital photographs of the as-prepared film before and after UV irradiation.

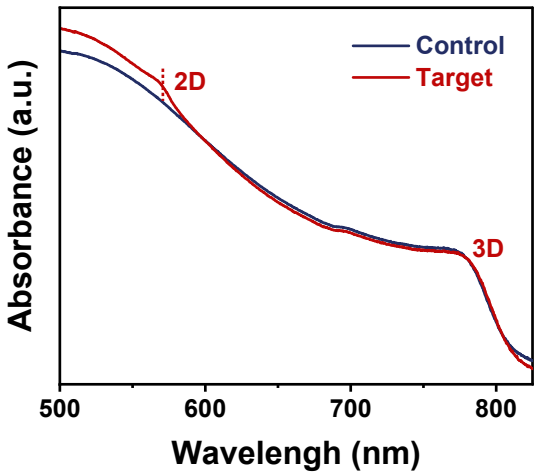

Fig. S6 UV-vis absorption spectra of the control film and the heterojunction film. Compared with the control film, the heterojunction film shows not only the characteristic absorption of the 3D perovskite but also a distinct additional signal assigned to the phase-pure n=2 2D perovskite, confirming the formation of a phase-pure 2D/3D heterojunction.

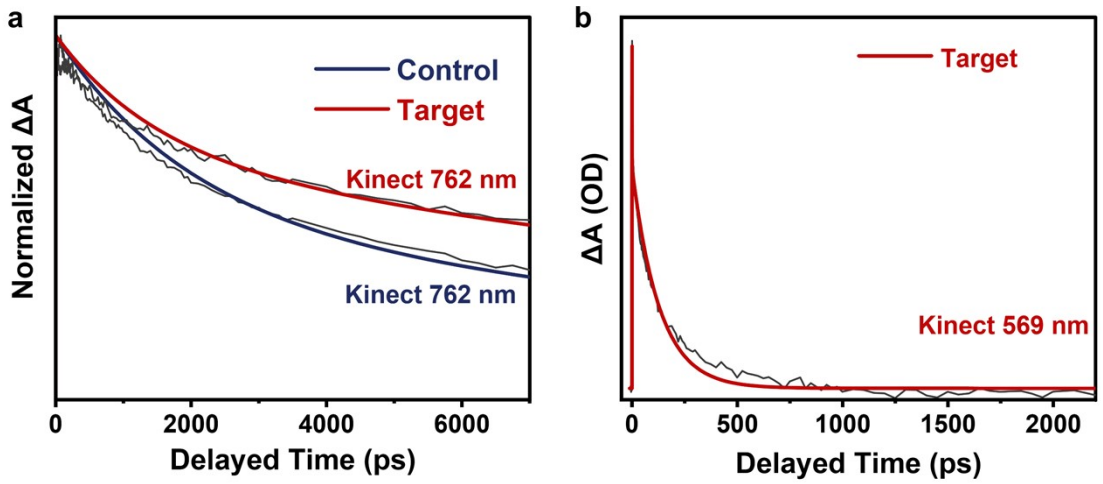

Fig. S7 TA kinetic traces were extracted at 762 and 569 nm to further investigate the carrier dynamics of the perovskite films. The 762 nm signal is assigned to the 3D perovskite component, whereas the 569 nm signal corresponds to the phase-pure 2D perovskite layer in the target film. As shown in Fig. S7a, the target film exhibits a slower decay of the 3D-related bleaching signal at 762 nm than the control film, indicating suppressed carrier recombination and reduced defect-assisted carrier loss in the 3D perovskite bulk.

In addition, the 2D-related signal of the target film monitored at 569 nm decays rapidly at early delay times and becomes weak at longer delays, as shown in Fig. S7b. This rapid decay reflects the depletion of carriers in the 2D surface layer. Together with the simultaneously prolonged 3D-related signal at 762 nm, these TA kinetics demonstrate carrier transfer from the 2D layer to the 3D perovskite bulk and confirm that the pure 2D/3D heterostructure in the target film promotes interfacial carrier transfer while suppressing nonradiative recombination.

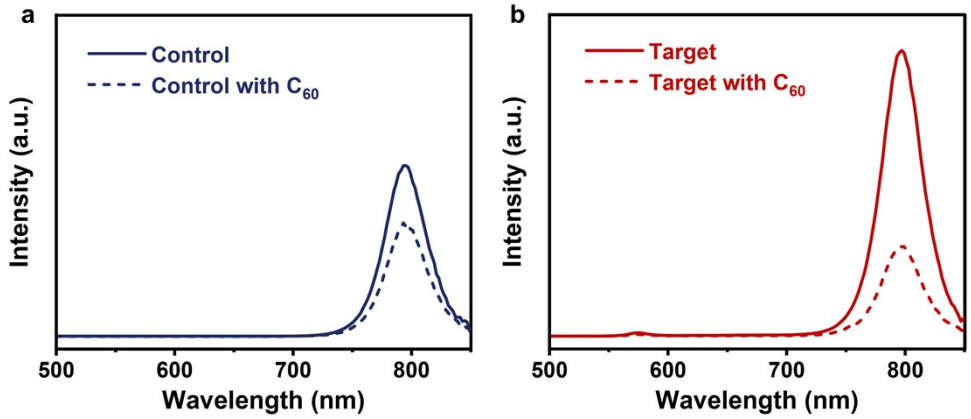

Fig. S8 Steady-state PL spectra of the (a) control and (b) target films before and after C_{60} deposition.

To evaluate whether the 2D layer affects charge extraction at the top interface, steady-state PL spectra were measured before and after C60 deposition. After C60 was deposited on the perovskite surface, both the Control and Target films exhibited obvious PL quenching, confirming charge transfer from the perovskite absorber to the C60 electron transport layer. Notably, the PL quenching ratio increased from 0.37 for the Control film to 0.68 for the Target film, indicating more efficient interfacial charge extraction in the Target film. This result suggests that the

ultrathin 2D layer formed on the 3D perovskite surface does not block carrier transport. Instead, it suppresses surface recombination and maintains effective charge extraction across the 2D/3D heterojunction.

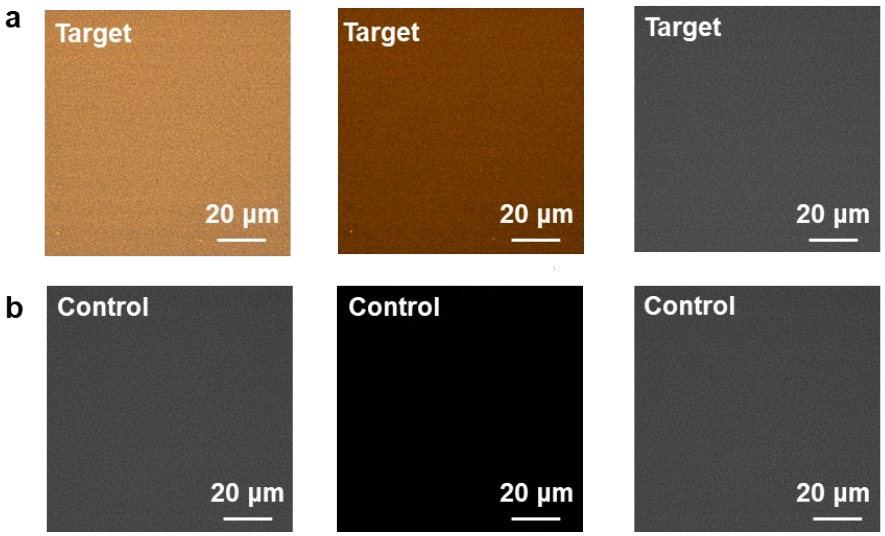

Fig. S9 Merged images, fluorescence-channel images, and bright-field microscopic images of the control film and the target film collected by laser confocal microscopy in the 560-600 nm detection window. In this range, the target film shows a clear fluorescence signal, whereas the control film is essentially non-emissive, further supporting the formation of the 2D (n = 2)/3D heterojunction after molecular imprinting.

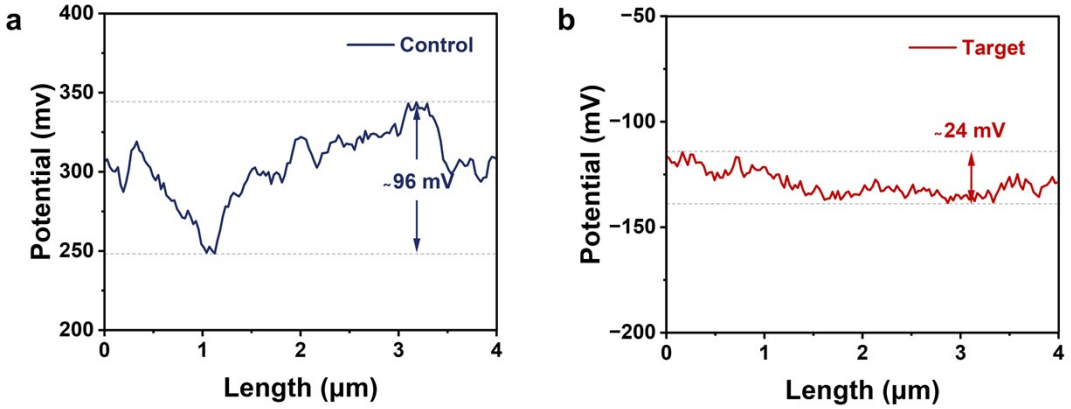

Fig. S10 Surface-potential distributions of the control film and the target film derived from the KPFM measurements. The target film shows a clear shift toward lower potential values together with a narrower distribution.

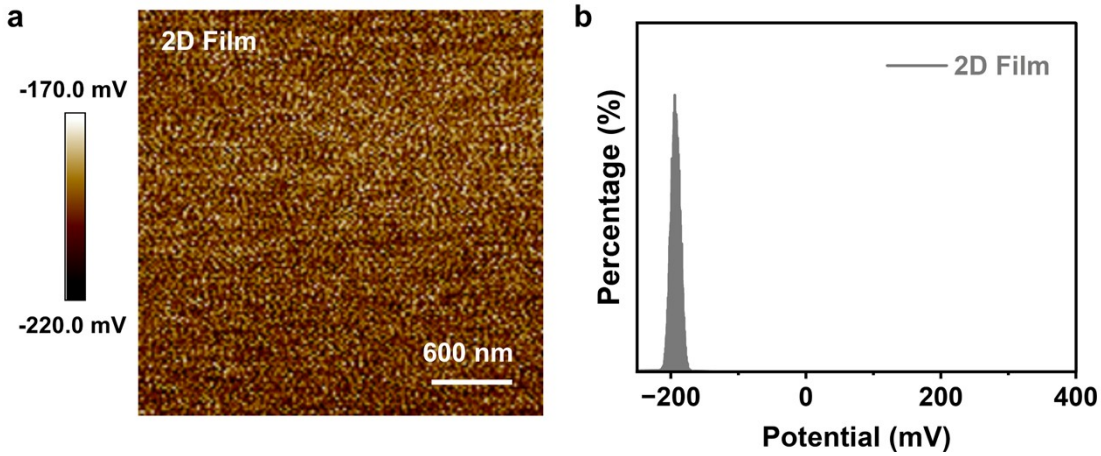

Fig. S11 (a) KPFM surface potential maps and (b) surface potential distributions of the phase-pure 2D films.

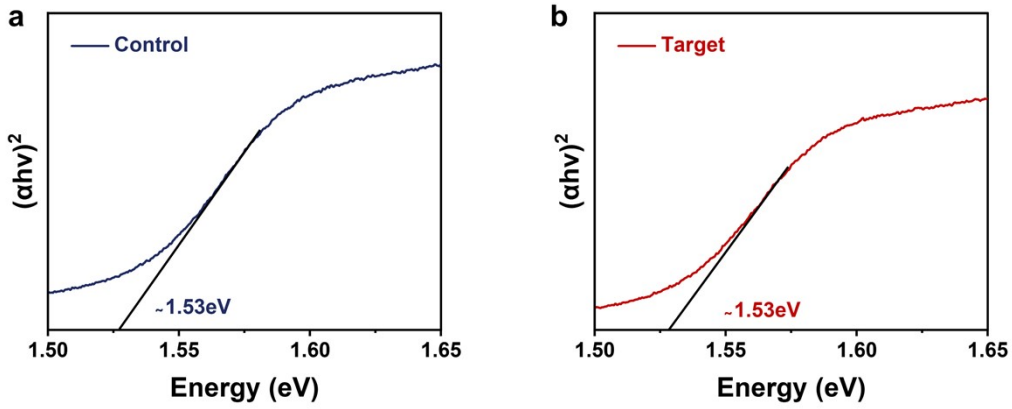

Fig. S12 UV-vis absorption spectra of the control film and the target film used for bandgap determination.

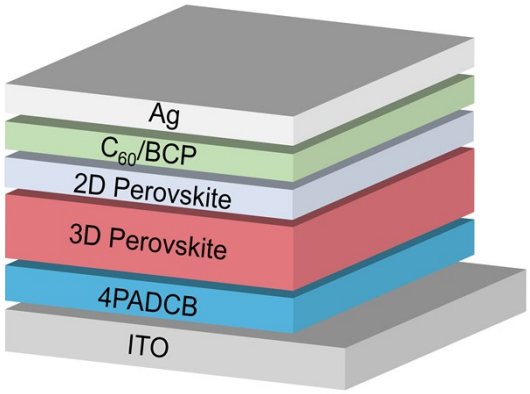

Fig. S13 Schematic diagram of the inverted device architecture.

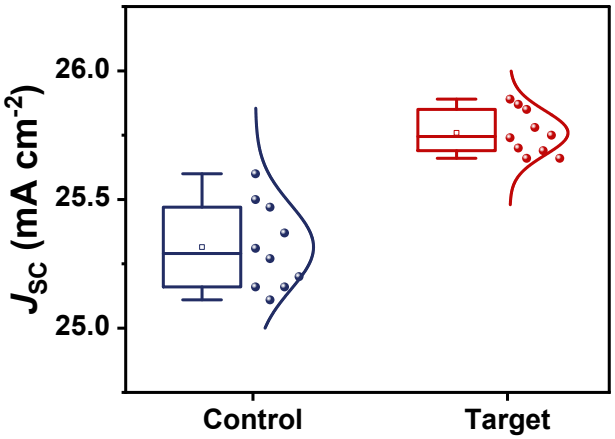

Fig. S14 Box-chart statistics of J_{SC} for the control and target devices.

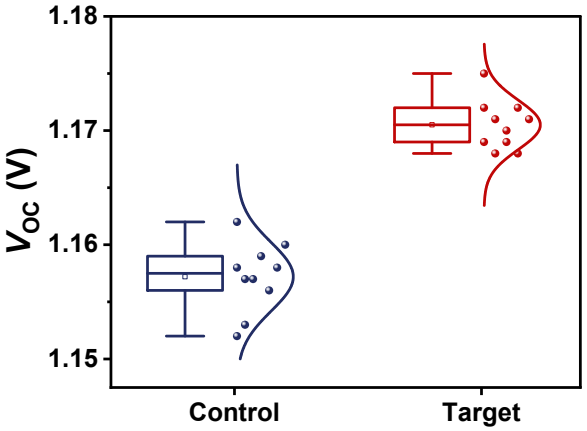

Fig. S15 Box-chart statistics of V_{OC} for the control and target devices.

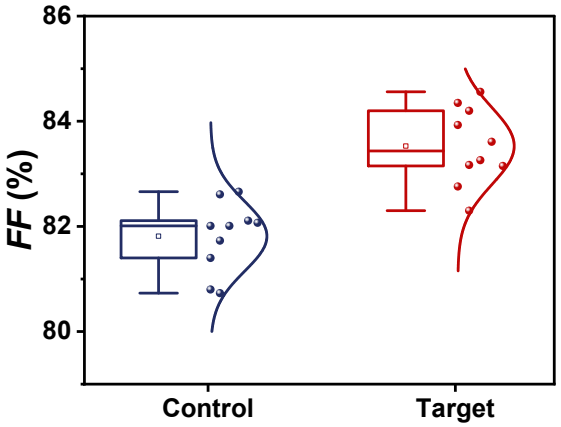

Fig. S16 Box-chart statistics of *FF* for the control and target devices.

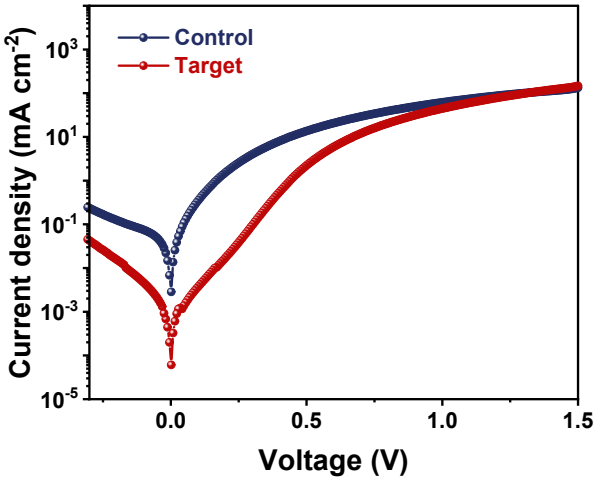

Fig. S17 Dark *J-V* curves compare the leakage current behavior between the control and target devices.

The reduced dark current of the target solar-cell device indicates a lower density of defect states. Under dark bias, defects can serve as recombination centers for injected electrons and holes, thereby increasing the recombination-related dark current. Therefore, the reduced dark current in the target device suggests suppressed defect-assisted recombination. This behavior is different from that observed in the SCLC measurements, where the increased current in electron-only devices reflects reduced trap-limited transport barriers and improved electron transport rather than enhanced leakage.

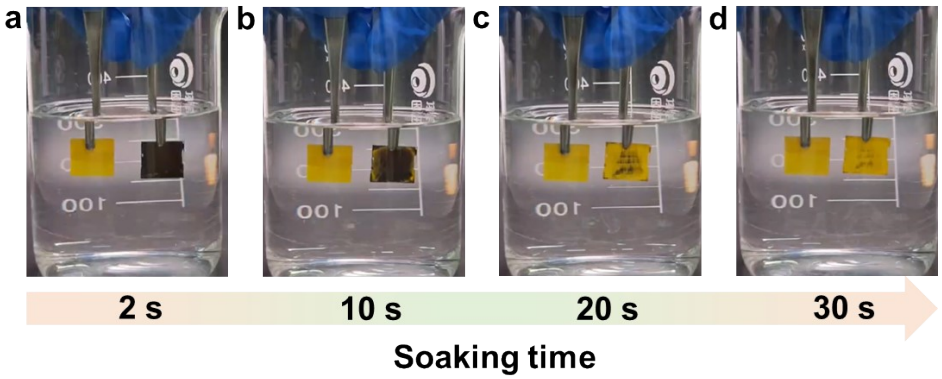

Fig. S18 Digital photographs of the target film (left) and the control film (right) after soaking in water for 2 s (a), 10 s (b), 20 s (c), and 30 s (d), showing the much better water tolerance of the target film during water exposure.

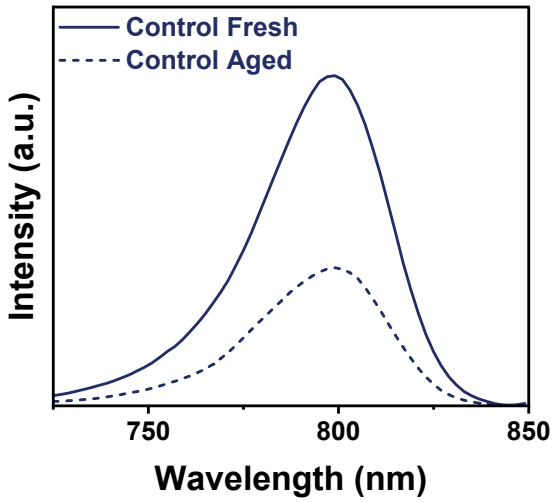

Fig. S19 PL spectra of the fresh and aged control films. The aged film was stored at room temperature under 60% relative humidity for 100 h before measurement.

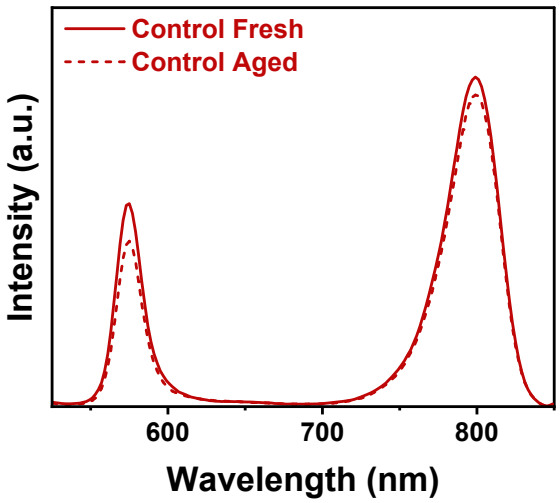

Fig. S20 PL spectra of the fresh and aged target films. The aged film was stored at room temperature under 60% relative humidity for 100 h before measurement.

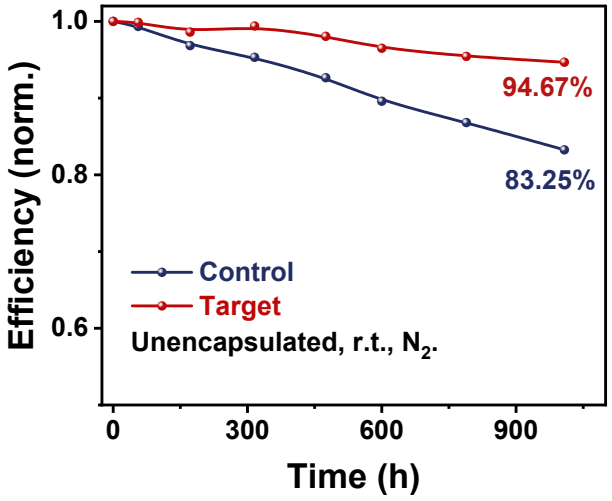

Fig. S21 Normalized efficiency evolution of the unencapsulated control and target devices stored in N_2.

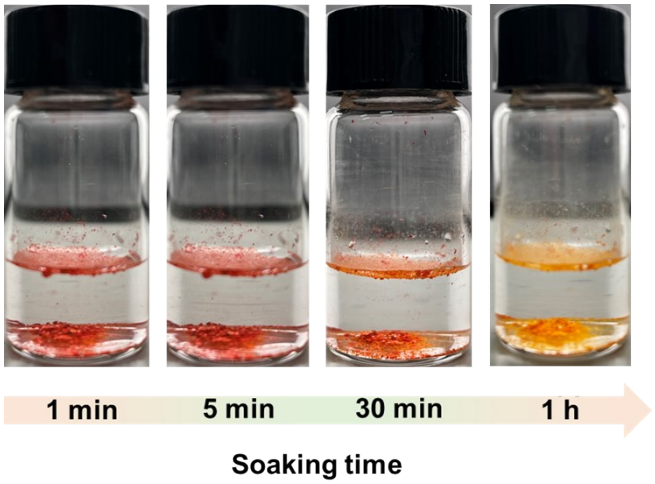

Fig. S22 Digital photographs of the as-prepared 2D single crystal after soaking in water for 1 min, 5 min, 30 min, and 1 h, showing the time-dependent changes during water exposure.

To further clarify the origin of this enhanced water stability, phase-pure 2D single crystals were immersed in water and photographed at different time intervals. Their preserved morphology confirms the intrinsic water tolerance of the DA-derived 2D phase, indicating that the improved water resistance of the imprinted film mainly arises from the 2D perovskite formed on the top surface.

References.

1. I. Spanopoulos, I. Hadar, W. Ke, Q. Tu, M. Chen, H. Tsai, Y. He, G. Shekhawat, V. P. Dravid, M. R. Wasielewski, A. D. Mohite, C. C. Stoumpos and M. G. Kanatzidis, *J. Am. Chem. Soc.*, 2019, **141**, 5518-5534.